Sustainable Engineering Materials
ISSN: 3105-1960 (Print); ISSN: 3105-1979 (Online)
http://www.sustain-dpl.com/picnews.asp?id=177
DOI: 10.54113/j.suem.2026.000019

ORIGINAL ARTICLE

Dowel-bearing properties of bolted joints in eucalyptus-based wood scrimber composites: an experimental and numerical investigation

Yuxuan Wang[a,b,c], Haitao Li[a,b,c*], Yijia Guo[d], Jingru Zhang[a,b,c], Haitao Ke[e], Priscilla Omouendze Mouaragadja[f], Pin Zhou[e], Yougui Luo[a,b,c], Shan Zhao[g], Rodolfo Lorenzo[h]

[a]Jiangsu Carbon Sequestration Materials and Structural Technology of Bamboo & Wood Research Center, Nanjing Forestry University, Nanjing 210037, China
[b]National-provincial joint engineering research center of biomaterials for MACHINERY PACKAGE, Nanjing Forestry University, Nanjing 210037, China
[c]College of Civil Engineering, Nanjing Forestry University, Nanjing 210037, China
[d]School of International Education, Tianjin Chengjian University, Tianjin 300384, China
[e]Anhui HanZhiYuan Technology Co., Ltd., Suzhou 234009, China
[f]National College for Water and Forestry of Gabon, Libreville 3960, Gabon
[g]Nanjing Zidong Investment Development Group Co., Ltd., Nanjing 210000, China
[h]University College London, London WC1E 6BT, UK
*Corresponding Author: Haitao Li, Professor. Email: lhaitao1982@126.com

Abstract: Understanding the dowel-bearing behavior of engineered wood products is essential for the design of reliable mechanical connections in sustainable timber structures. This study investigates the embedment performance of eucalyptus-based wood scrimber (EBWS), a high-density and low-carbon engineered composite, under various dowel diameters and loading directions. A total of 240 specimens were tested using both half-hole and full-hole embedment methods across four orthotropic configurations. The influence of dowel diameter, loading orientation, and test configuration on bearing strength and initial stiffness was analyzed. Finite element simulations incorporating the Hill yield criterion and localized "weak zones" were conducted using ABAQUS to capture stress evolution and failure mechanisms. Results show that dowel diameter significantly affects stiffness and strength evolution, and that half-hole tests yield higher and more stable embedment performance than full-hole tests. The findings provide experimental insight and modeling strategies for the reliable application of EBWS in dowel-connected structural systems.

Keywords: dowel-bearing strength, eucalyptus-based wood scrimber, failure mechanisms, finite element modeling

1 Introduction

Engineered timber and bamboo structures are attracting increasing attention in sustainable architecture due to their renewability, low embodied carbon, and exceptional strength-to-weight ratios [1-3]. In such structures, mechanical connections—particularly dowel-type bolted joints—play a critical role in the overall load-bearing behavior [4-7]. The performance of these joints significantly governs the structural integrity, stiffness, and failure modes of the entire assembly. Among the key mechanical parameters characterizing bolted joints, the dowel-bearing strength and initial embedment stiffness of the wood or bamboo substrate are of fundamental importance [8]. These parameters not only influence joint strength but also affect energy dissipation, deformation capacity, and load transfer

Received: 24 December 2025; Received in revised form: 4 May 2026; Accepted: 28 May 2026

efficiency. As such, accurate characterization of dowel-bearing performance is indispensable for joint design, numerical modeling, and performance-based safety assessment in modern timber and bamboo buildings.

Wood scrimber products fabricated from fast-growing species offer a sustainable pathway to reduce dependency on old-growth timber while maximizing mechanical efficiency. At present, the main species used for structural engineered wood is poplar [9-12], a widely cultivated species in China. In order to expand the choice of species, eucalyptus was chosen as the raw material for the production of reconstituted wood in this study. Eucalyptus-based wood scrimber (EBWS), manufactured from hybridized eucalyptus cultivated in southern China, has shown initial potential as a load-bearing member in structural building engineering [13]. The production process of EBWS comprises flaking, drying, adhesive impregnation, cold pressing, and thermal curing. Moreover, the utilization of eucalyptus—a plantation species with a short growth cycle—aligns with global carbon neutrality goals and makes EBWS a viable candidate for low-carbon construction systems, particularly in dowel-connected timber or hybrid structures. However, there is currently no research evaluating the mechanical properties of EBWS, especially its connection properties as structural components.

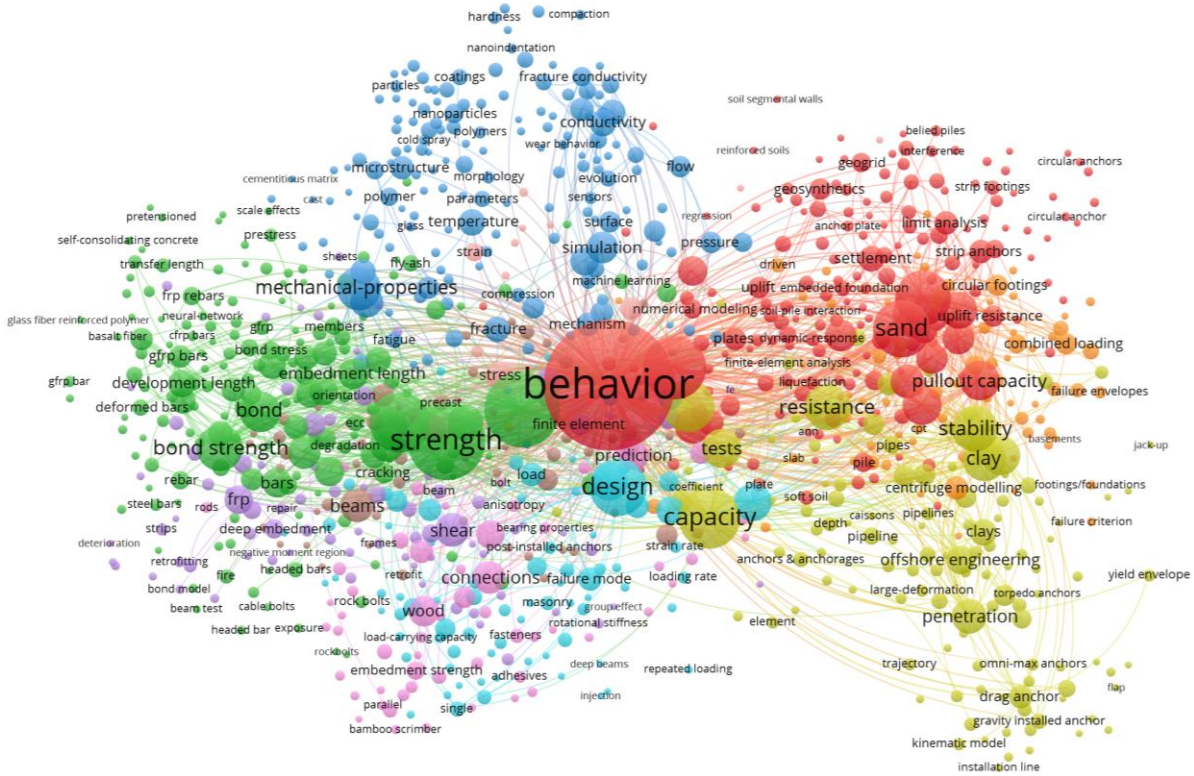

Fig. 1. Keyword co-occurrence network based on the search terms “dowel-bearing properties” or “embedment behavior,” generated using VOSviewer.

Recent studies have increasingly focused on the embedment behavior of structural materials under mechanical loading, as evidenced by the prominence of the keyword "behavior" in literature-based visualizations [14-16]. As shown in the keyword co-occurrence map (**Fig. 1**), research has developed into several thematic directions: geotechnical studies (red cluster) emphasize pullout capacity and limit analysis, while work on fiber-reinforced polymers and rebar systems (green cluster) highlights bond strength and embedment length. Particularly relevant to this study is the wood-focused cluster (purple), where dowel-bearing strength, adhesive behavior, and failure modes are key research themes. Within the context of timber structures, prior studies have demonstrated that dowel-bearing strength and initial stiffness are influenced by multiple factors, including geometric parameters (e.g., dowel diameter and embedment length), material anisotropy, loading direction (parallel vs. perpendicular to the grain), and moisture content [17]. When dowel slot specimens meet the minimum dimensional requirements specified in design standards, size effects on mechanical properties are often negligible [18]. However, some studies have identified a diameter-dependent size effect, wherein increasing the dowel diameter

improves stiffness but may reduce bearing strength due to stress dispersion and reduced lateral confinement [19].

Recent advancements in finite element modeling (FEM) have significantly improved the understanding of embedment behavior in wood- and bamboo-based connections [20-21]. Wood scrimber is produced using impregnation and reconstruction techniques and is considered a typical composite material. Due to structural inhomogeneities—such as microcracks and weaknesses at glue interfaces—wood often exhibits early yielding or localized damage in regions of high stress concentration [20]. By defining a "foundation region" within the FEM framework, the effects of these localized defects on the overall load-bearing capacity can be more accurately captured, leading to better alignment between simulation and experimental results. For instance, Leng et al [22] proposed a nonlinear FEM approach to simulate the dowel-bearing performance of engineered bamboo, analyzing how the shape and size of the foundation region affect simulation accuracy. Similarly, Karagiannis [23] applied the foundation region concept to simulate dowel-bearing behavior in glued laminated timber, validating the FEM outputs against Digital Image Correlation (DIC) data with good agreement. Compared to solid wood or laminated timber, EBWS exhibits significantly higher density, pronounced fiber orientation, and a layered microstructure formed through compression and adhesive consolidation. These characteristics are likely to influence its local failure modes and stress distribution under embedment loading. Therefore, it is essential to adapt FEM techniques—including material modeling, contact definitions, and damage criteria—to accurately reflect the mechanical response of wood scrimber joints.

Although existing research has advanced the understanding of traditional timber and glulam systems, it may not fully reflect the mechanical behavior of EBWS—a high-density, wood scrimber composite with distinct structural characteristics. Due to its special raw composition, fiber alignment and manufacture process, EBWS may respond differently under embedment loading. However, studies specifically addressing its dowel-bearing and embedment behavior remain limited. In this study, a total of 240 specimens were fabricated and tested using both half-hole and full-hole embedment methods across four different fiber arrangement combinations and dowel diameters (from 12 mm to 20 mm). In addition, the stress evolution and failure mechanisms were analyzed using ABAQUS finite element modeling based on the Hill anisotropic yield criterion, where a localized "weak zone" was introduced to better simulate stress concentration near the dowel slot. This comprehensive study aims to provide a reliable dataset and modeling framework for the design, optimization, and predictive simulation of EBWS connections in modern timber or hybrid structures.

2 Materials and methods

2.1 Materials

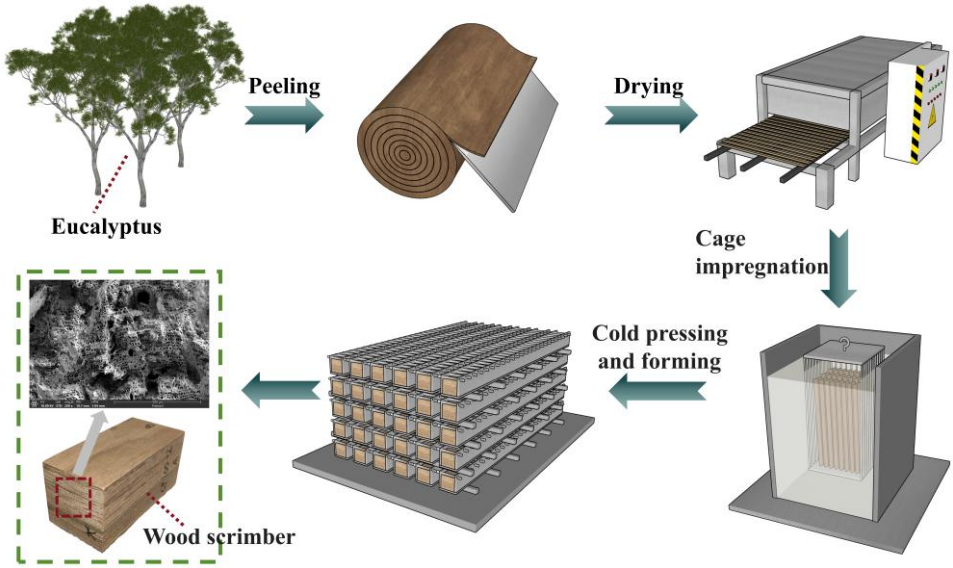

Fig. 2. Manufacture process of specimens.

The eucalyptus-based wood scrimber (EBWS) utilized in this study was manufactured from five-year-old hybridized clonal Eucalyptus trees cultivated in Guangxi Province, China. The EBWS specimens were produced by Jiangsu Hanzhiyuan Environmental Protection Technology Co, Ltd. As illustrated in **Fig. 2**, the fabrication process included mechanical debarking, flaking into thin veneers, drying, adhesive impregnation using a cage immersion method, mat consolidation by cold pressing, and subsequent thermal curing. This process resulted in a highly densified, fiber-aligned composite with enhanced mechanical uniformity (**Fig. 2**). The finalized EBWS panels were then trimmed and cut into dowel-bearing test specimens. The average air-dry density of the specimens was approximately 1.00 g/cm³, determined based on their mass and dimensions.

The basic mechanical properties of the EBWS were tested according to ASTM-D143-14 [24]. A comparison was made between the results of the EBWS basic mechanical properties tests and those of engineered bamboo and timber materials as reported in the literature.

As shown in **Table 1**, EBWS exhibits a relatively high density compared with most engineered wood and bamboo products reported in the literature, indicating the strong densification effect introduced during manufacturing. In particular, its longitudinal compressive and tensile strengths are comparable to or higher than those of many conventional engineered materials, suggesting strong potential for load-bearing structural applications. However, the marked differences between the longitudinal and transverse properties also confirm the pronounced anisotropy of EBWS. This anisotropic behavior is expected to significantly influence the embedment response of dowel-type connections, which further justifies the need for the present study on loading direction-dependent dowel-bearing behavior.

Table 1. Comparison of mechanical properties between eucalyptus-based wood Scrimber and other engineered bamboo and wood materials.

Materials	Density (kg/m³)	(MPa)	Compression			Tension			Shear	Bending	
			L	R	T	L	R	T		R	T
Eucalyptus-based wood scrimber (this study)	1002	Strength	98.71	37.88	—	142.4	3.77	—	12.95	137.5	
		modulus	14816	1127	—	19780	1279	—	2480	16895	
Poplar scrimber[25]	780-940	Strength	101.0	18.0	24.0	108.0	2.0	4.0	17.0	140.0	
		modulus	16870	1167	1317	11069	—	—	—	22310	
Birch plywood[26]	693	Strength	31.3	23.9	—	62.5	56.7	—	11.9	—	
		modulus	11900	9400	—	9400	6700	—	610	—	
Laminated bamboo lumber[27]	689	Strength	75.1	20.5	—	128.2	8.1	—	14.7	—	—
		modulus	9914	1854	—	11294	2371	—	1165	—	—
Bamboo scrimber[28]	1254	Strength	100.9	52.8	—	156.2	3.88	—	26.7	144.3	
		modulus	14160	4313	—	15649	—	—	—	9919	
Thermally modified beech timber[29]	650	Strength	48.7	6.2		14.4	—		—	30.8	
		modulus	9300	—		16700	—		—	16600	

2.2 Experimental Design and Mechanical test protocol

The mechanical properties of EBWS were calculated based on 5 %-diameter off-set method recommended by ASTM D5764 [30]. To eliminate the initial interference (due to gaps in the loading contact surfaces and lack of compression of the specimen), this calculated standard requires the stiffness be determined by originally estimating a value of Px, completing a linear regression analysis on the force–displacement curve in the range of Px and Px+30%. After that, the fitted straight line was offset by 5%-d, and the longitudinal coordinate of the intersection with the load-displacement curve was defined as the yield strength. The initial embedment stiffness (ke) and the dowel-bearing strength (fe) were evaluated for each test based on formulas in **Fig. 3**.

A schematic of the two test methods is shown in **Fig. 4**. Different test methods significantly affect the mechanical response and measured dowel-bearing capacity of wood-based materials. In the half-hole configuration, Stress distribution is relatively uniform and compressive, promoting vertical load transfer with minimal shear interaction. In contrast, stress distribution in the full-hole test is less confined, with significant lateral expansion and potential dowel rotation, reducing load concentration

efficiency. As reported in the study, the half-hole test is advised for hardwoods and engineered wood products whose embedment strength is higher than the dowel yield moment; in all other cases, the full-hole test is advised. Therefore, in this study we used two test methods separately to investigate the effect of loading pattern on dowel-bearing mechanical behavior.

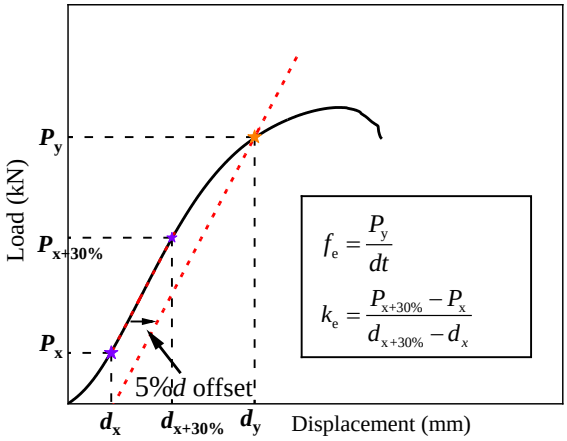

Fig. 3. Parameter calculation method.

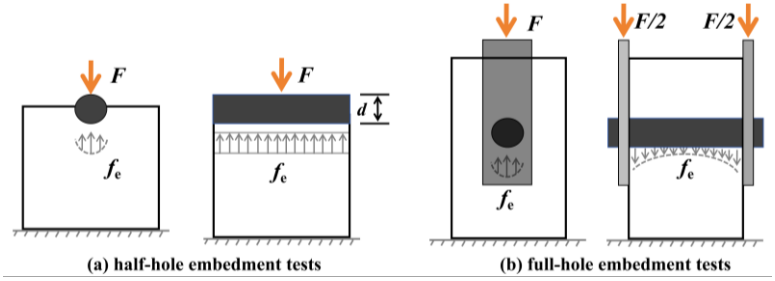

Fig. 4. Stress distribution of the two test setups: (a) half-hole set and (b) full hole set.

Dowel diameter and loading direction were the main factors considered in this study. **Fig. 5(a)** illustrates the material orientation of EBWS. The specimen identification follows the format "M + loading direction + dowel orientation + dowel diameter". For instance, "MLRD12" refers to a specimen subjected to loading along the longitudinal (L) direction, with the dowel oriented in the radial (R) direction, and a dowel diameter of 12 mm. It is worth noting that in specimen groups such as "MLRF", the final letter "F" denotes the use of the full-hole embedment method, in which the dowel diameter is fixed at 16 mm.

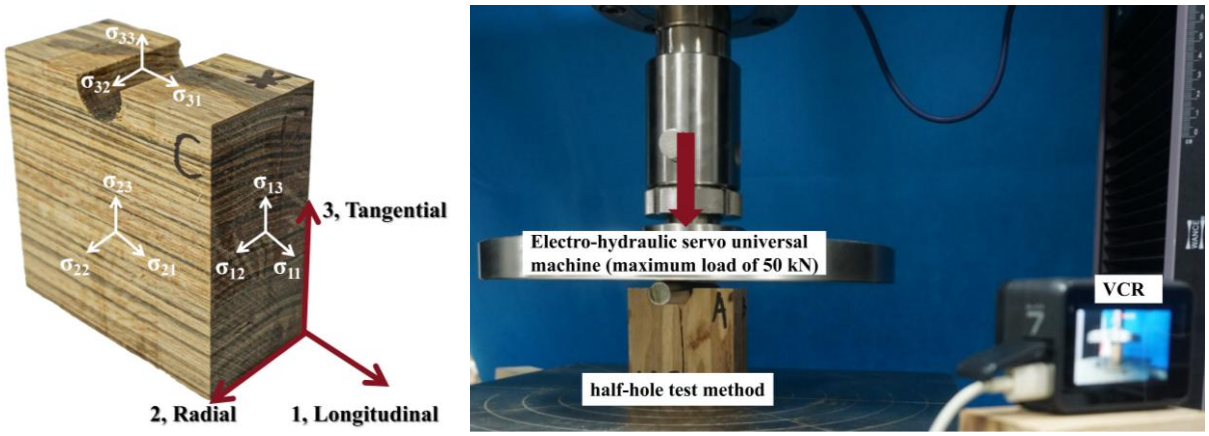

(a) EBWS's material directions and stress components

(b) Loading process

Fig. 5. EBWS's material directions and loading process

To research the influence of the diameter of dowel in dowel-bearing properties, this paper set different diameter (d=12 mm, 14 mm, 16 mm, 18 mm, 20 mm) of the dowels for all different loading direction group. It is important to note that all half-hole specimens were set to the same dimensions

(L = 80 mm, W = 80 mm, T = 40 mm), also all full-hole specimens were set to the same dimensions (L = 80 mm, W = 80 mm, T = 40 mm). It is worth mentioning that the diameter of the hole was 1.5 mm larger than the bolt diameter.

The test loading facility is shown in **Fig. 5(b)**. The load method adopted was displacement control with a speed of 1.5 mm/min. All the tests were finished by a SANS universal testing machine with a maximum load of 50 kN. All specimens are put into the constant temperature and humidity box in advance (temperature of 20 ℃ and relative humidity (RH) of 65%) to ensure the stability and uniformity of the test environment.

2.3 Numerical Simulation Method

The development of rational numerical models to predict the mechanical properties of structures is critical for design. Wood Scrimber is a typical anisotropic material with different mechanical properties in different directions. In numerical simulation, in order to simplify the calculation, the bamboo and wood materials are usually simplified as orthotropic anisotropic materials for simulation calculation. Hill yield criterion is a commonly used criterion to describe the yielding behavior of anisotropic materials such as metals, composites and wood. It is established based on the yielding surfaces of anisotropic materials, and is particularly applicable to materials with mechanical properties in different directions. Unlike the classical Von Mises yield criterion, the Hill yield criterion takes into account the stress-strain behavior of the material in different directions, thus better describing the yield properties of the material under different loading directions. As shown in **Fig. 6**, ε_{yt} is the transverse compressive yield strain, ε_{xt} is the cis tensile yield strain, ε_{yc} is the transverse compressive yield strain, and ε_{xc} is the cis compressive yield strain.

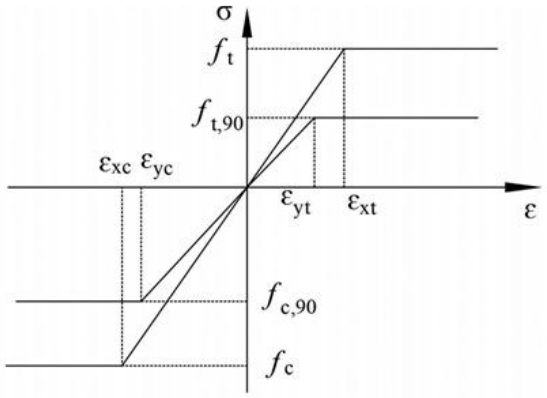

Fig. 6. Ideal elastic-plastic constitutive relation model.

Hill yield theory defines the yield surface for orthotropic materials by incorporating directional dependence of mechanical properties, thereby offering improved accuracy in predicting failure under multi-axial stress states. The general form of the Hill criterion is expressed as Eq. (1-8):

$$F(\sigma_{ij}) = \sqrt{F(\sigma_{22}-\sigma_{33})^2 + G(\sigma_{33}-\sigma_{11})^2 + H(\sigma_{11}-\sigma_{22})^2 + 2L\sigma^2_{23} + 2M\sigma^2_{31} + 2N\sigma^2_{12}} < \sigma^0 \quad (1)$$

Where F, G, H, L, M, N are material-dependent parameters derived from the basic mechanical tests in different material directions. These coefficients are formulated in terms of normalized strength ratios: R_{11}, R_{22}, R_{33}, R_{12}, R_{13}, R_{23} are the plastic strength coefficients of the material.

$$F = \frac{\sigma_0^2}{2}\left(\frac{1}{\overline{\sigma}_{22}^2} + \frac{1}{\overline{\sigma}_{33}^2} - \frac{1}{\overline{\sigma}_{11}^2}\right) = \frac{1}{2}\left(\frac{1}{R_{22}^2} + \frac{1}{R_{33}^2} - \frac{1}{R_{11}^2}\right) \quad (2)$$

$$G = \frac{\sigma_0^2}{2}\left(\frac{1}{\overline{\sigma}_{33}^2} + \frac{1}{\overline{\sigma}_{11}^2} - \frac{1}{\overline{\sigma}_{22}^2}\right) = \frac{1}{2}\left(\frac{1}{R_{33}^2} + \frac{1}{R_{11}^2} - \frac{1}{R_{22}^2}\right) \quad (3)$$

$$H = \frac{\sigma_0^2}{2}\left(\frac{1}{\overline{\sigma}_{22}^2} + \frac{1}{\overline{\sigma}_{33}^2} - \frac{1}{\overline{\sigma}_{11}^2}\right) = \frac{1}{2}\left(\frac{1}{R_{11}^2} + \frac{1}{R_{22}^2} - \frac{1}{R_{33}^2}\right) \quad (4)$$

$$L = \frac{1}{2}\left(\frac{\tau_0}{\overline{\sigma}_{23}^{2}}\right)^2 = \frac{3}{2R_{23}^2} \tag{5}$$

$$M = \frac{1}{2}\left(\frac{\tau_0}{\overline{\sigma}_{13}^{2}}\right)^2 = \frac{3}{2R_{13}^2} \tag{6}$$

$$N = \frac{1}{2}\left(\frac{\tau_0}{\overline{\sigma}_{12}^{2}}\right)^2 = \frac{3}{2R_{12}^2} \tag{7}$$

$$\begin{cases} R_{11} = \dfrac{\overline{\sigma}_{11}}{\sigma_0}, R_{22} = \dfrac{\overline{\sigma}_{22}}{\sigma_0}, R_{33} = \dfrac{\overline{\sigma}_{33}}{\sigma_0}, R_{12} = \dfrac{\overline{\sigma}_{12}}{\tau_0}, R_{13} = \dfrac{\overline{\sigma}_{13}}{\tau_0}, R_{23} = \dfrac{\overline{\sigma}_{23}}{\tau_0} \\ \tau_0 = \dfrac{\sigma_0}{\sqrt{3}} \end{cases} \tag{8}$$

The material constitutive model was defined in the ABAQUS property module based on the results of material characterization tests. Previous studies have shown that the mechanical behavior of wood in the two transverse directions is generally comparable [25]. Therefore, the material characterization tests in this study were limited to the longitudinal (L) and radial (R) directions. In the subsequent analysis, it was assumed that the compressive strength of the recombined wood in the radial (R) and tangential (T) directions was equivalent. **Table 2** shows the basic mechanical parameters of all material. In the finite element software, steel is defined as an ideal elastic-plastic material, and its elastic modulus and Poisson's ratio are set to 210000MPa and 0.25 respectively. The bending yield strength is determined based on the bolt test.

Table 2. FEM material parameter values

	Direction	EBWS	Bolt	Steel plate/Steel Base
Modulus (MPa)	E11	14815	210000	210000
	E22	802	210000	210000
	E33	802	210000	210000
Poisson's ratio	ν12	0.45	0.25	0.25
	ν13	0.45	0.25	0.25
	ν23	0.05	0.25	0.25
Shear Modulus (MPa)	G12	2414	—	—
	G13	2414	—	—
	G23	1212	—	—
Bending strength (MPa)	f_y	—	600	500

3 Test results and discussion

The average values of the Dowel-bearing strength, initial embedment stiffness and air-dry density in each group are taken as shown in **Table 3**. The coefficients of variation (COV) for almost all experimental groups are within 20%, reflecting relatively stable mechanical properties with excellent reliability of its dowel-bearing strength and embedded initial stiffness. The air-dry densities of all half-hole and full-hole specimens stabilized around 1 g/cm3, indicating that the shape of the specimen had a negligible effect on the density. Based on the measured dowel-bearing properties, discussions in terms of the failure modes, the influence of dowel diameter, loading direction, and test setups are made in the following sections.

3.1 Influence of factors on dowel-bearing properties

3.1.1 Effect of bolt diameter and loading direction for half-hole specimens

The dowel-bearing properties of different loading directions and different dowel diameters have been synthesized in **Fig. 7**. The plot incorporates both raw test data (scattered points) and the corresponding

mean values (trend lines).

Table 3. Test results

Group	Diameter (mm)	Dowel-bearing strength (MPa)	COV	Initial embedment stiffness (kN/mm)	COV	Air-dry density (g/cm^3)
MLRD-1	12	105.85	3.09%	49.78	4.72%	1.04
MLRD-2	14	101.02	5.74%	48.55	14.37%	1.06
MLRD-3	16	97.85	4.31%	53.46	18.81%	0.97
MLRD-4	18	99.77	3.00%	68.46	4.44%	1.01
MLRD-5	20	102.08	5.60%	69.49	4.45%	1.01
MLRF	16	79.36	3.56%	26.53	12.24%	1.05
MLTD-1	12	66.88	11.66%	49.08	10.24%	1.03
MLTD-2	14	65.25	4.23%	49.98	11.16%	1.03
MLTD-3	16	66.36	5.49%	52.99	6.16%	0.98
MLTD-4	18	68.95	6.60%	55.92	6.49%	1.01
MLTD-5	20	62.93	8.47%	60.45	6.04%	1.02
MLTF	16	73.74	4.90%	30.14	17.94%	1.03
MRTD-1	12	91.49	7.95%	20.42	2.71%	1.00
MRTD-2	14	81.06	6.89%	21.05	10.65%	1.01
MRTD-3	16	79.96	3.06%	21.67	6.18%	1.00
MRTD-4	18	73.88	3.85%	23.33	10.45%	0.97
MRTD-5	20	69.16	6.69%	24.38	6.10%	0.99
MRTF	16	63.41	6.90%	17.35	10.56%	0.99
MTRD-1	12	69.88	6.97%	15.41	2.50%	1.00
MTRD-2	14	66.88	7.16%	14.41	6.78%	1.00
MTRD-3	16	64.33	6.36%	13.74	5.04%	0.97
MTRD-4	18	64.01	6.50%	14.94	5.50%	0.98
MTRD-5	20	62.93	7.09%	17.32	6.96%	0.96
MTRF	16	50.08	7.17%	13.29	5.51%	0.97

For all half-hole specimen groups, the dowel-bearing strength exhibits a non-monotonic trend with increasing dowel diameter (**Fig. 7** (**a, b, c, d**)). For LR group, specifically, a slight decline is observed when the diameter increases from 12 mm to 14 mm, followed by a modest recovery at diameters of 18 mm and 20 mm (**Fig. 7** (**a**)). For the other groups, there was an overall trend of decreasing strength with increasing dowel diameter. Similar conclusions were obtained by Yang, Zhang. This behavior can be attributed to a combination of stress concentration, anisotropic load transfer, and glue-line interaction effects: For smaller dowels (e.g., 12, 14mm), stress is concentrated within a narrow contact area, potentially leading to locally high compressive stress and apparent higher bearing strength. However, as the diameter increases, stress becomes distributed over a larger area, but the stress transfer efficiency diminishes due to the laminated fiber structure, resulting in a decrease in effective bearing capacity. For larger dowels, the load is transferred across a broader glue line region. If the glue penetration is uneven or interfacial bonding is suboptimal, stress voids and early interfacial failure may occur, further contributing to the drop in strength.

In contrast, the overall initial embedment stiffness of all specimens showed a significant increase with increasing dowel diameter (**Fig. 7**(**a, b, c, d**)). There is a clear trend of increasing stiffness with increasing dowel diameter when loaded parallel to the grain. In contrast, the trend of increase is not significant and almost negligible when loaded perpendicular to the grain. This reflects the improved load distribution and enhanced contact response at the early stages of loading: Larger dowel diameters inherently increase the bearing interface, which reduces local deformation and improves stiffness during the elastic loading phase. On the other hand, as the dowel diameter increases, the system stiffness (EI) also increases, enhancing resistance to local indentation and facilitating a more uniform stress field. The load is more evenly transmitted across the cross-section, thereby postponing the onset of localized yielding and allowing a wider range of linear elastic deformation, which increases the apparent stiffness.

For **Fig. 7**(**e, f**)), dowel-bearing properties are stronger for parallel loading than for perpendicular loading, and R-direction loading is stronger than T-direction loading. This is due to the fact that when loaded in the T-direction, the wood bonding layer has more defects leading to weakened properties.

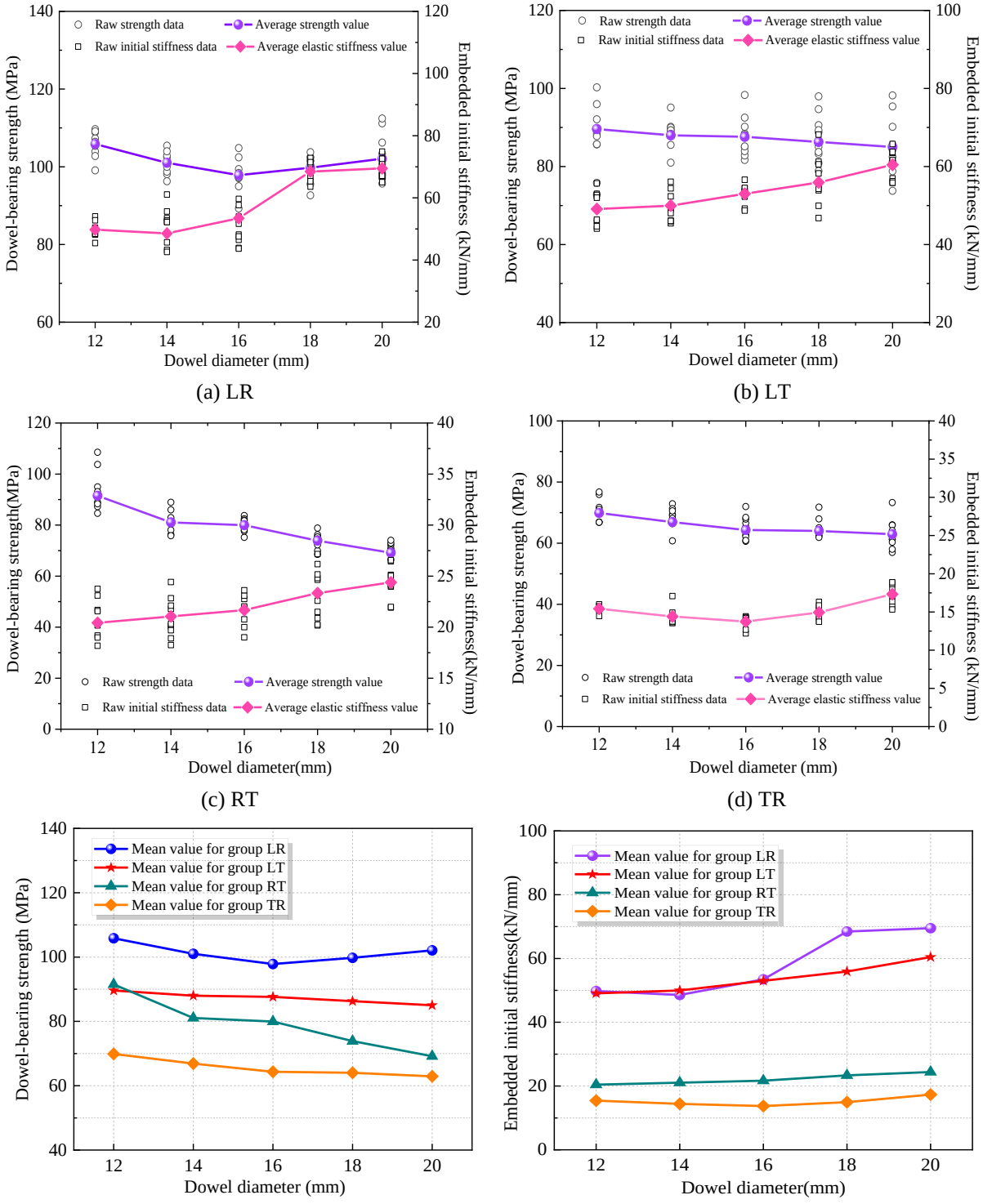

Fig. 7. Dowel-bearing properties under different dowel diameters.

3.1.2 Effect of test method

Fig. 8 provides a comparative evaluation of dowel-bearing strength and initial embedded stiffness between two commonly employed test configurations: the half-hole embedment test and the full-hole embedment test. Both raw values and relative percentage differences are presented.

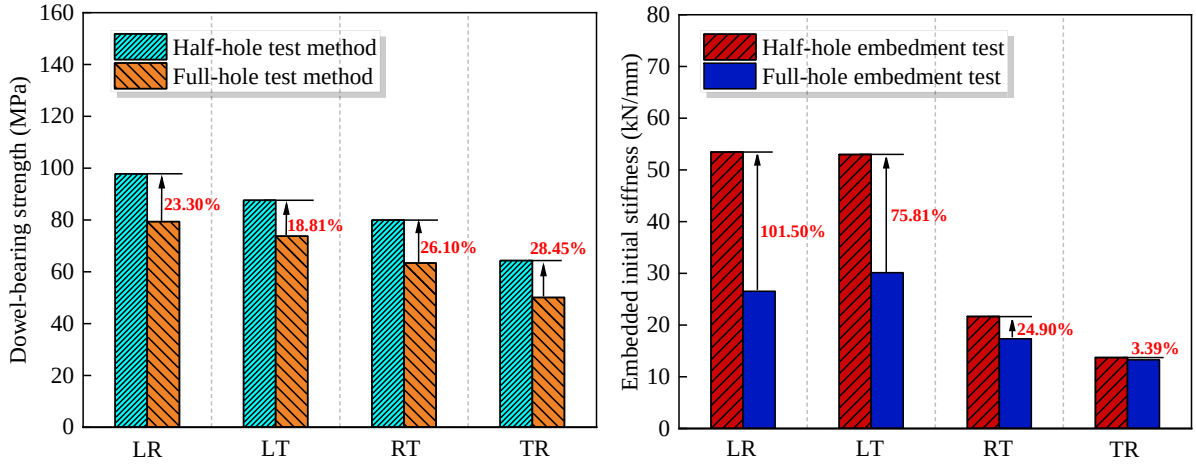

(a) Dowel-bearing strength comparisons (b) Initial embedment stiffness comparisons

Fig. 8. Dowel-bearing properties under different test methods.

Across all loading configurations, the half-hole test consistently yields higher dowel-bearing strength than the full-hole test, with relative increases ranging from ~18.8% to 28.5%. In contrast, the effect of test configuration on initial stiffness is even more pronounced. In the LR and LT configurations, the initial stiffness from the half-hole test is approximately 101.5% and 75.8% higher, respectively, than that from the full-hole test. For TR and RT, the increases are more moderate (24.9% and 3.4%). The half-hole configuration allows the applied load to be more effectively transferred into the specimen through a flat reaction surface, leading to reduced rotational freedom of the dowel and more uniform stress distribution across the contact arc. Full-hole specimens are more prone to complex 3D deformation, including dowel rotation and asymmetric fiber compression, which reduces the effective bearing area and leads to premature fiber crushing or interfacial failure. In the half-hole test, the dowel is pressed against a rigid, flat bearing surface, which ensures higher contact stiffness at the early loading stage. In contrast, full-hole tests allow for micro-rotations and bedding-in effects that reduce the slope of the initial load–displacement curve. These findings emphasize that the test method has a significant impact on the measured embedment performance. The half-hole configuration is mechanically more favorable in terms of constraining deformation, producing higher apparent strength and stiffness, and thus may better represent in-situ dowel loading conditions in real joints.

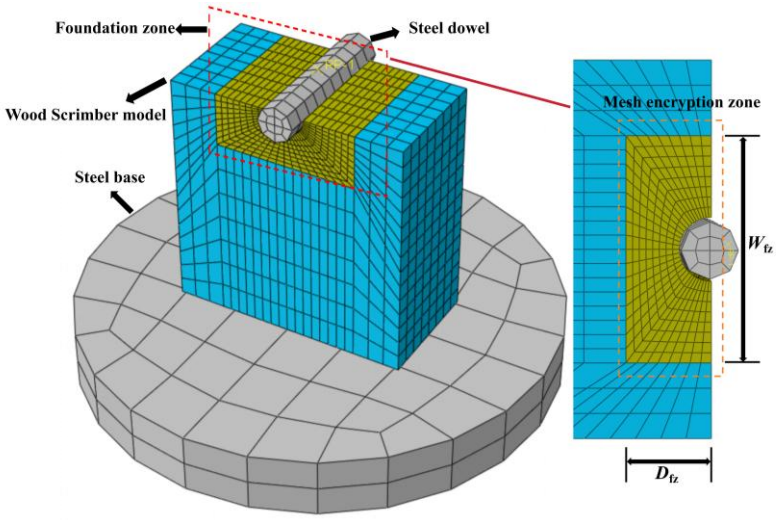

Fig. 9. FEM model of the half-hole specimens with foundation zone.

3.2 Analysis of the Numerical Model

3.2.1 Model information

As is shown in **Fig. 9**, detailed 3D models were constructed by means of the FEM program ABAQUS. The model consists of three primary components: the EBWS specimen, the steel dowel, and a rigid steel base. The EBWS is modeled as a solid continuum with orthotropic mechanical properties, while the steel dowel and base are represented as elastic-plastic materials with significantly higher stiffness to emulate boundary constraints. The contact interaction between the steel dowel and the wood surface was simulated using surface-to-surface contact pairs, with the stiffer steel dowel defined as the master surface and the more compliant wood surface designated as the slave. To enhance numerical stability and reduce the risk of non-convergence, the default hard contact formulation for normal behavior was replaced with a linear pressure–overclosure relationship exhibiting a high penalty stiffness. Tangential behavior was modeled using a Coulomb friction law with a friction coefficient of μ = 0.7, as recommended by Smith [31]. Quasi-static loading was applied by prescribing incremental downward displacements to the nodes at both ends of the dowel along the global y-axis, while the corresponding vertical reaction forces were extracted from the fixed base nodes to generate the load–displacement response.

Referring to the modified foundation modeling strategy reported in previous studies on timber and engineered bamboo connections, a localized zone surrounding the dowel hole was therefore introduced to represent the weakened material domain [22]. A key feature of the modeling approach is the introduction of a localized mesh refinement (encryption) around the dowel hole, designated as the mesh encryption zone. The zone surrounding the dowel hole is also defined as a material softening region (weak zone) to account for the degradation in strength and stiffness due to stress concentrations and potential micro-cracking. The main timber volume, excluding the localized weak zone, was assigned average orthotropic material properties derived from the previous experimental campaign. In contrast, the weak zone surrounding the dowel hole was modeled with reduced stiffness and strength parameters to account for localized damage and stress concentrations. The reduction factors used to define the degraded properties were based on experimentally determined weakening ratios, as detailed in the accompanying Eq. (9-10). The weak zone correction factor is shown in the **Table 4**. Notably, only the compressive strength and elastic modulus were modified in the weak zone based on test data, while Poisson's ratio and shear modulus were retained at their original values, assuming minimal sensitivity to localized material degradation.

$$\frac{E_{11,\mathrm{fz}}}{E_{11,\mathrm{ini}}} = \frac{E_{22,\mathrm{fz}}}{E_{22,\mathrm{ini}}} = \frac{E_{33,\mathrm{fz}}}{E_{33,\mathrm{ini}}} = \alpha \tag{9}$$

$$\frac{f_{11,\mathrm{fz}}}{f_{11,\mathrm{ini}}} = \frac{f_{22,\mathrm{fz}}}{f_{22,\mathrm{ini}}} = \frac{f_{33,\mathrm{fz}}}{f_{33,\mathrm{ini}}} = \beta \tag{10}$$

Table 4. Material correction factor for foundation area

Group	d(mm)	α	β	Specimen group	d(mm)	α	β
Parallel to the grain (half-hole set)	12	0.14	0.91	Perpendicular to the grain (half-hole set)	12	0.3	0.71
	14	0.20	0.81		14	0.54	0.71
	16	0.27	0.86		16	0.47	0.81
	18	0.20	0.86		18	0.47	0.91
	20	0.21	0.96		20	0.51	0.86

3.2.2 Comparison of stress distribution maps and failure mode

To investigate the stress evolution mechanism of the dowel-bearing properties by half-hole set, a series of finite element simulations were conducted using bolt diameters of 12, 14, 16, 18, and 20 mm in **Fig. 10**. As the dowel diameter increases, a pronounced expansion of the stress concentration zone can be observed in both loading directions. Specifically, in the longitudinal direction, stress intensification occurs at the arc-shaped edge of the dowel slot, indicating a typical shear-splitting failure initiation. When d=18mm and d=20mm, stress levels near the dowel corners exceed 90 MPa, approaching the local compressive strength, confirming the model's ability to capture yielding and plastic deformation zones. In contrast, the transverse specimens exhibit a more dispersed stress field centered around the dowel axis, with high-stress zones confined primarily to the fiber contact region

under the bolt. This pattern corresponds well to compressive crushing and localized buckling failure modes. The observed stress distribution supports the definition of a "foundation zone" around the dowel slot, as proposed in the modified foundation model. Stress contours exhibit a radial gradient, with peak stress values diminishing sharply beyond approximately 1.5–2 times the bolt radius. This affirms the rationality of defining a lower-modulus, lower-yield-strength zone in the finite element model to better match experimental failure morphology.

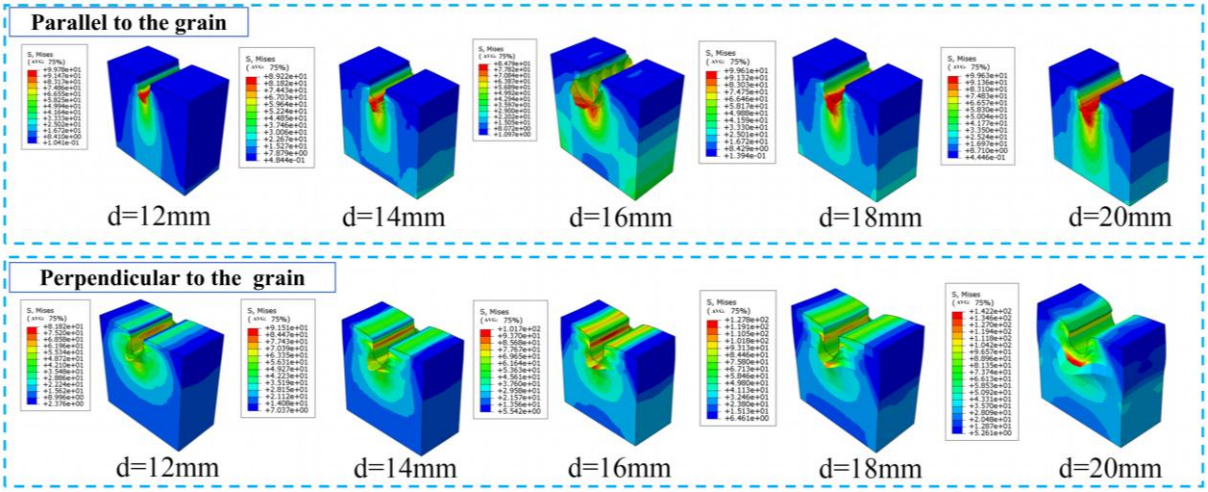

Fig. 10. Stress distribution in EBWS dowel slots under varying bolt diameters

To further elucidate the failure mechanism of dowel-embedded recombined wood, Figure 11 juxtaposes the experimentally observed fracture patterns with corresponding finite element simulation results and stress trajectory sketches. Two dominant failure modes are identified: Failure Mode I — Longitudinal Shear-Splitting (**Fig. 11**(**a-d**)), and failure Mode II — Transverse Compressive Crushing (**Fig. 11**(**e-h**)).

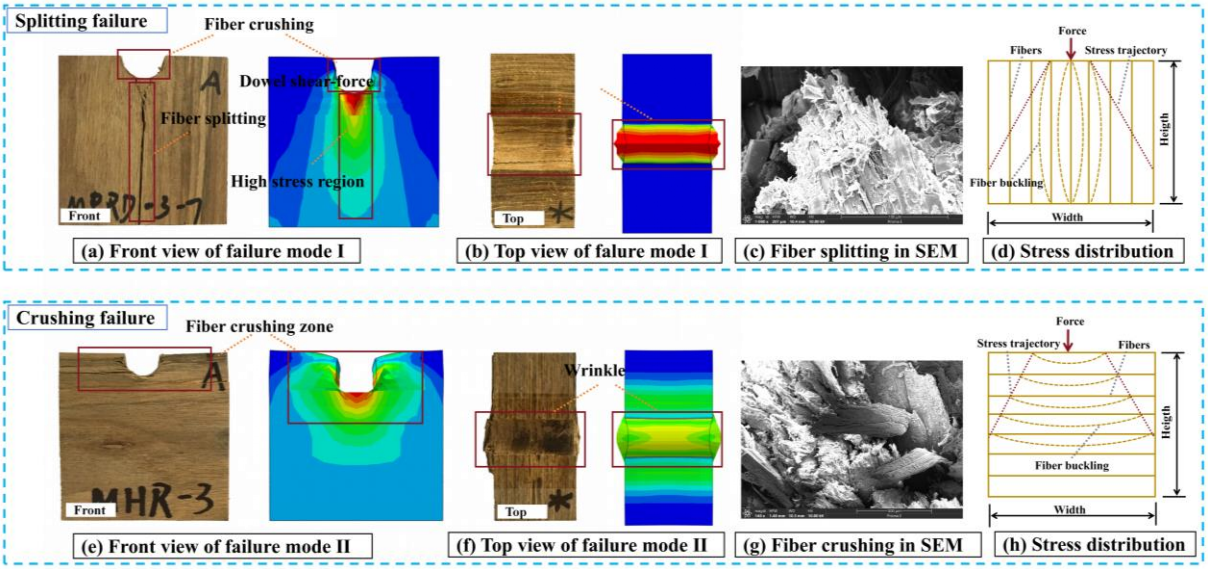

Fig. 11. Comparison of simulated stress distribution and specimen failure mode

Specimens loaded in the L-direction exhibit prominent splitting cracks (**Fig. 10**(**a**)). A combination of fiber tearing, interlaminar shear, and splitting delamination is observed, indicating tensile failure induced by stress concentration at the dowel contact edge. Simulated stress distribution exhibits an elongated, high-stress band (~90 MPa) aligned with the loading direction, coinciding precisely with the experimentally observed crack path (**Fig. 10**(**b**)). The region directly beneath the arc of the slot shows maximum stress accumulation, validating the mechanical initiation of the splitting failure. A scanning electron microscope (SEM) was used to take a photo of the wood fiber being pulled out (**Fig. 11**(**c**)), and macroscopic cracking and damage occurred in this area on the surface.

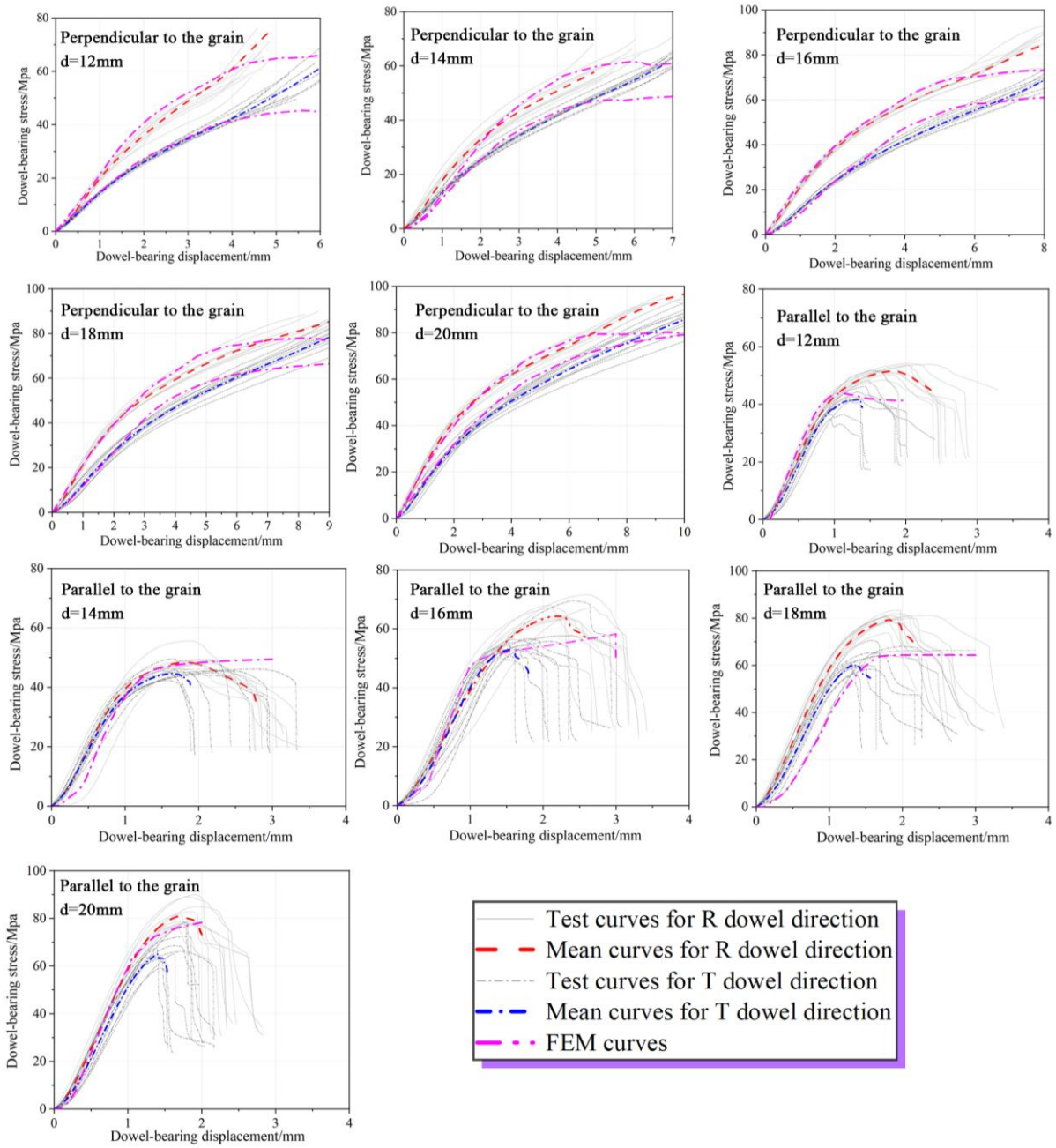

Fig. 12. Comparison of experimental and numerical curves.

In contrast, specimens subjected to loading perpendicular to the grain display dense crushing, wrinkling, and localized compaction beneath the dowel arc (**Fig. 11**(**e**)). No extended cracks are present, and failure manifests as plastic deformation rather than catastrophic fracture. Numerical results reveal a symmetric, ellipsoidal high-stress zone (~130 MPa), matching well with the wrinkled and compacted failure morphology observed experimentally (**Fig. 11**(**f**)). The stress concentration is broader but shallower compared to Mode I, consistent with crushing and yielding of short transverse fibers. Under SEM observation, structural disintegration of the cellular architecture was evident due to compressive crushing failure. The thin-walled tissue appeared nearly "densified," and irregular cracks were observed on the fractured surface. Fiber bundles on the loaded surface were also crushed and separated from the surrounding parenchyma, with distinct inter-fiber separation observed among wood fibers (**Fig. 11**(**g**)).

As illustrated schematically in **Fig. 11** (**d, h**), different mechanisms of load resistance are exhibited by areas of high deformation, both between parallel-to-grain and perpendicular-to-grain orientations.

Under parallel-to-grain loading, large deformations initiate local buckling in the vertical wood fibers located directly beneath the dowel (**Fig. 11(d)**). As the load increases, the neighboring fibers offer confinement, thereby further concentrating the deformation in the buckling region. This mechanism results in the progressive engagement of more material along the loading direction, thereby promoting the splitting failure. In contrast, under perpendicular-to-grain loading, displacement tends to localize within the upper fibers, while the lower fibers behave like an elastic foundation. Once yielding initiates in the upper layers, non-linear deformation primarily concentrates near the top surface and propagates horizontally along the grain direction **Fig. 11(h)**. This behavior reflects the anisotropic stress redistribution typical of transverse embedment in wood-based materials.

3.2.3 Comparison of stress cloud map and failure mode

Fig. 12 presents a comparison between the finite element method (FEM) output and the experimentally obtained stress–displacement curves. In the numerical model, orthotropic material directions were varied to simulate different grain orientations. Notably, for specimens subjected to loading parallel to the grain, only a single FEM curve is shown due to the experimental assumption that the compressive strengths in the R and T directions are equivalent. The simulated curves exhibit a strong agreement with the experimental paths, particularly in the elastic stage, where stress trajectories align closely. This consistency confirms that the introduction of the weak zone in the model effectively captures the stress concentration behavior observed in the bearing failure of dowel-embedded joints.

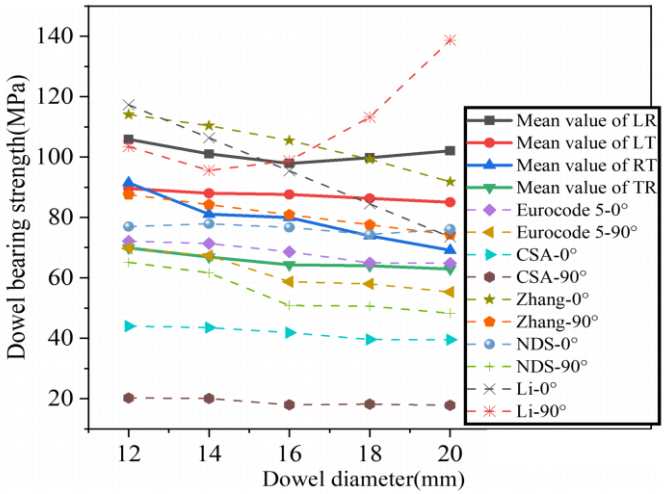

Fig. 13. The comparison between predicted dowel-bearing strength and test mean value.

Table 5. The calculation methods of dowel-bearing strength.

Standard or literature	Formula	
	Parallel-to-grain	Perpendicular-to-grain
Eurocode 5	$f_{e,0}=0.082(1-0.01d)\,p_k$	$f_{e,90}=0.082(1-0.01d)\,p_k / K_{90}$
CSA	$f_{e,0}=50G(1-0.01d)$	$f_{e,90}=22G(1-0.01d)$
Zhang	$f_{e,0}=(-0.0016d^2+0.023d+1.11)\,f_{c,0}$	$f_{e,90}=(-0.044d+2.84)\,f_{c,90}$
NDS	$f_{e,0}=77.27G$	$f_{e,90}=212G^{1.45}d^{-0.5}$
Li	$f_{e,0}=[-0.554(\frac{d}{10})+1.853]\,f_{c,0}$	$f_{e,90}=[3.673(\frac{d}{10})^2-10.59(\frac{d}{10})+10.15]\,f_{c,90}$

Notes: d is the bolt diameter (mm); G is the density of timber (g/cm3); p_k is the characteristic density; f_c,0 is the Dowel bearing strength parallel to the fiber (MPa); f_c,90 is the Dowel bearing strength perpendicular to the fiber (MPa). K_{90} is Adjustment coefficient, K_{90}=0.90+0.015d (Hardwood).

3.3 The calculation methods for dowel-bearing strength and initial stiffness

3.3.1 Existing calculation methods testing for the dowel-bearing strength

To calculate the dowel-bearing strength, current standards and publications primarily focus on the compressive strength of timber or take into account the effects of density and bolt diameter. The **Table 5** presents the representative calculation methods for comparing the dowel-bearing strength of various ways on EBWS specimens, and the results illustrated in the **Fig. 13**. Most of these calculations underestimated the pin slot loading performance of the EBWS. This can be attributed to the difference between the density (Most materials in the literature have densities below 1 g/cm3). In the study of the dowel-bearing properties of bamboo scrimber [32] (density closest to EBWS), it was found that the construction of equations based on the correlation between the compressive strength and dowel diameter of the material had satisfactory predictive results. Hence, we attempt to construct equations that can be used to predict the strength of the EBWS. These equations will serve as a guide for the structural application of the EBWS, as discussed in the next subsection.

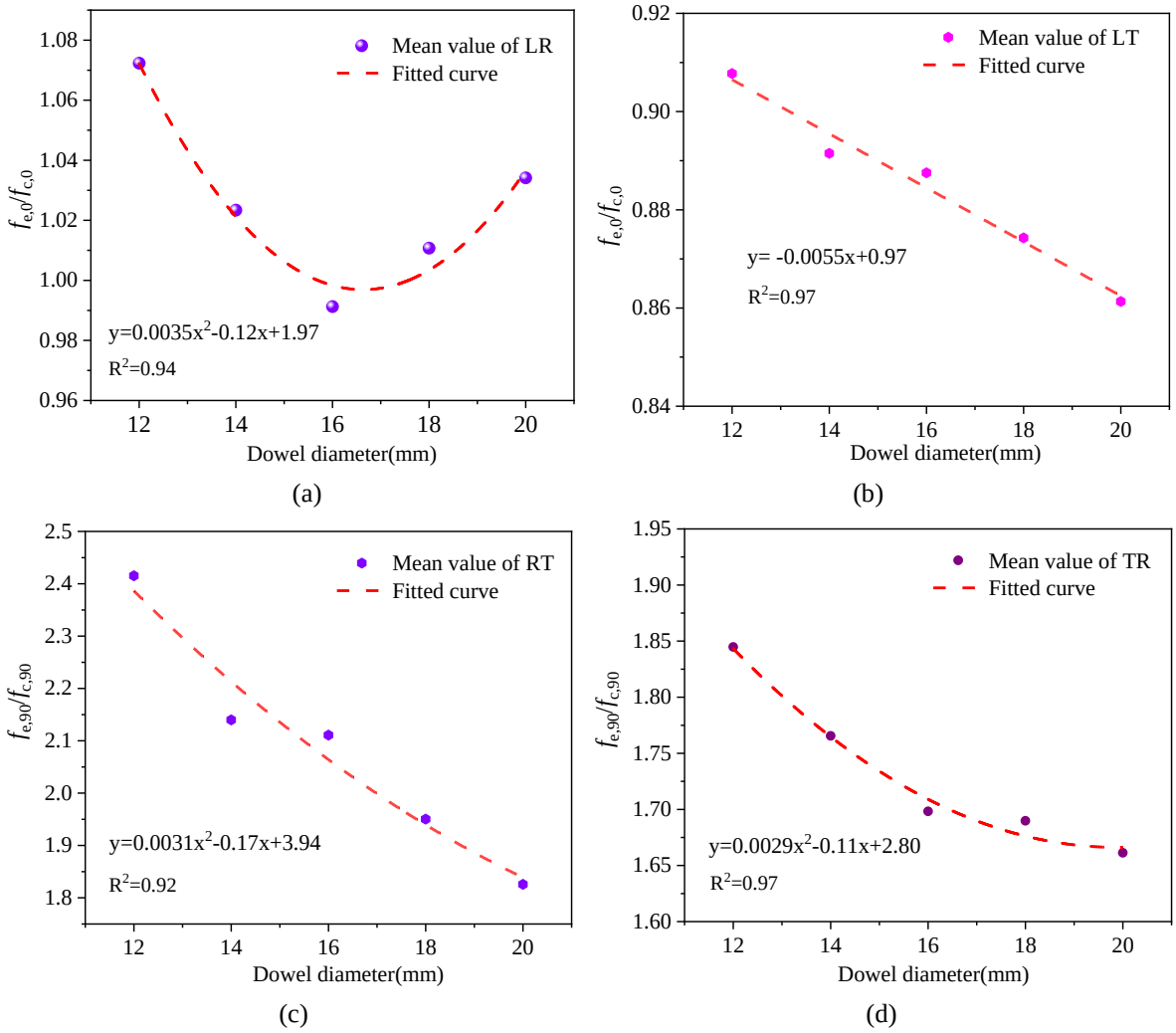

Fig. 14. The relationship between the ratio of dowel-bearing strength and compressive strength along with the dowel diameters.

3.3.2 The proposed formula for dowel-bearing strength of EBWS

Based on the analysis above, the aim of this paper is to analyze the impact of dowel diameters on dowel-bearing strength of EBWS and develop accurate formulas for predicting strength in different loading directions.

$$f_{e,y} = K_a f_c \tag{11}$$

Where $f_{e,y}$ is the predicted dowel-bearing strength (MPa) of EBWS; K_a is the influence coefficients of dowel diameter; f_c is the compressive strength.

By fitting experimental data (Mean value), **Fig. 14** displays the relationship between the ratio of dowel-bearing strength and compressive strength along with the dowel diameters. Eq. (12), an empirical equation can be formulated for determining the dowel-bearing strength of EBWS.

Where, $f_{c,0}$ and $f_{c,90}$ are the compressive strength of EBWS with fiber angles of 0° and 90°; According to the **Table 1**, $f_{c,0}$ and $f_{c,90}$ are taken as 98.71MPa and 37.88MPa respectively.

$$f_{ey}=\begin{cases}[0.35(\frac{d}{10})^2+1.2(\frac{d}{10})+1.97]\,f_{c,0} & \text{(LR)}\\ (-0.0055d+0.97)\,f_{c,0} & \text{(LT)}\\ [0.31(\frac{d}{10})^2+1.7(\frac{d}{10})+3.94]\,f_{c,90} & \text{(RT)}\\ [0.29(\frac{d}{10})^2+1.1(\frac{d}{10})+2.80]\,f_{c,90} & \text{(TR)}\end{cases} \tag{12}$$

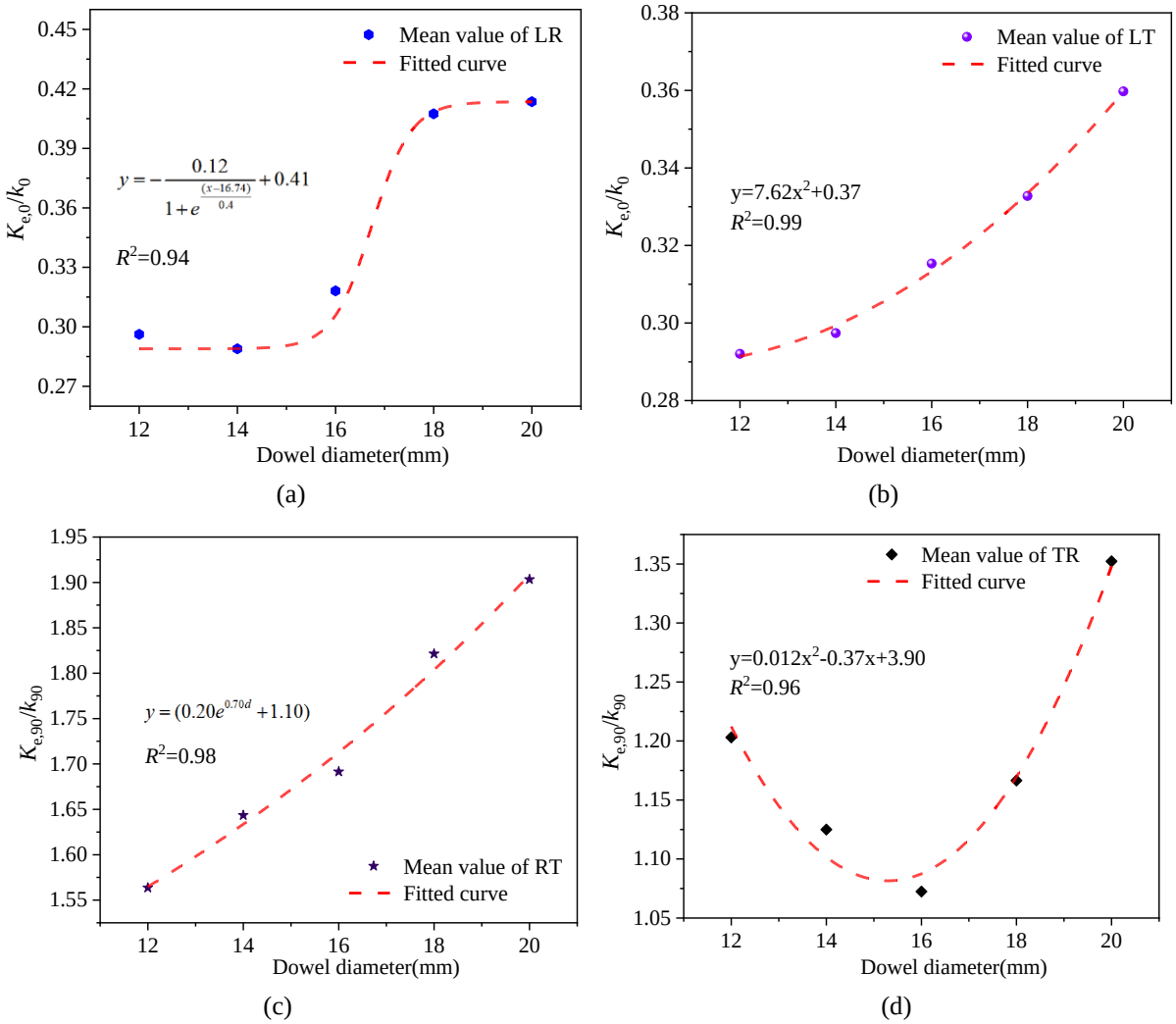

Fig. 15. The relationship between the ratio of embedment initial stiffness and compressive elastic strength along with the dowel diameters.

3.3.3 The proposed formula for embedded initial stiffness of EBWS

There are few existing standards or literature on methods for calculating the embedment initial stiffness of engineered bamboo or timber. Therefore, we have developed empirical equations based on Eq. to predict EBWS stiffnesses.

$$k_e = K_b k_c \tag{13}$$

Where k_e is the predicted embedment initial stiffness (kN/mm) of EBWS; K_b is the influence coefficients of dowel diameter. K_c is the mean value of the compressive elastic stiffness of the material under pressure (determined by material property tests).

By fitting experimental data (Mean value), **Fig. 15** displays the relationship between the ratio of embedded initial stiffness and initial stiffness (determined by compressive tests) along with the dowel diameters. In the equation (14), k_0 and k_{90} are the compressive elastic stiffness of EBWS with fiber angles of 0° and 90°.

$$k_e = \begin{cases} [\dfrac{-0.12}{1+e^{\frac{(d-16.74)}{0.4}}} + 0.41]k_0 & (LR) \\ (7.62d^2 + 0.37)k_0 & (LT) \\ (0.20e^{0.70d} + 1.10)k_{90} & (RT) \\ [1.2(\dfrac{d}{10})^2 + 3.7(\dfrac{d}{10}) + 3.90]k_{90} & (TR) \end{cases} \tag{14}$$

4 Conclusions

This study presents a comprehensive experimental and numerical investigation on the dowel-bearing behavior of EBWS, a high-density engineered composite developed from hybridized fast-growing eucalyptus. A total of 240 specimens were tested under various dowel diameters and orthotropic loading directions using both half-hole and full-hole embedment methods. Mechanical parameters, including dowel-bearing strength and initial stiffness, were systematically evaluated. The effects of test configuration and material anisotropy were thoroughly analyzed. FEM incorporating the Hill yield criterion and a localized "weak zone" strategy was employed to simulate the stress evolution near the dowel-wood interface. The simulation results showed good agreement with experimental data and effectively revealed the role of stress concentration, confinement, and directional load transfer in different failure modes. The findings contribute valuable insights into the design and analysis of bolted joints in engineered bamboo-wood materials and support the potential of EBWS for structural applications in low-carbon timber construction.

1. The eucalyptus-based wood scrimber produced through an optimized fabrication process exhibits excellent mechanical performance. In particular, the highest dowel-bearing strength was recorded in the L (longitudinal) direction, reaching up to 105.85 MPa in the standard half-hole embedment test group, indicating strong potential for structural applications.
2. Among all tested configurations, the longitudinal-radial (LR) direction consistently demonstrated the highest dowel-bearing strength and initial stiffness, making it the most favorable orientation for dowel-connected joints in EBWS elements.
3. Two primary failure modes were identified: splitting and crushing. Failure patterns were classified as either shear-induced longitudinal splitting (dominated by tensile and shear stresses along the grain) or compression-induced crushing (predominant in transverse directions).
4. The choice of embedment test method significantly influences measured performance. Compared to the full-hole method, the half-hole test configuration resulted in higher dowel-bearing strength and greater initial stiffness due to enhanced confinement and constrained dowel rotation, suggesting its superiority for evaluating true embedment behavior.
5. Finite element modeling revealed the stress evolution mechanisms throughout the embedment process. By integrating FEM results with failure mode observations, the study clarified the progression of stress concentration beneath the dowel and the development of localized plastic zones, validating the use of anisotropic material models and weak-zone definitions.

From a practical perspective, the results of this study provide useful guidance for the design and numerical modeling of dowel-type joints in EBWS members, particularly in terms of selecting favorable loading orientations and appropriate embedment test methods. The superior bearing strength and stiffness observed in the LR configuration suggest that aligning the principal load transfer with the

longitudinal direction is beneficial for joint performance. Nevertheless, this study focused only on the local embedment behavior of single-dowel specimens and did not consider multi-fastener interaction, end distance effects, cyclic loading, moisture variation, or long-term service conditions. In addition, the full-hole configuration was only examined for the 16 mm dowel diameter, which limits broader comparisons across all diameters. Future studies should therefore extend the investigation to full joint assemblies and multi-bolt configurations, while also considering fabrication tolerances, spacing effects, edge distance, and environmental actions, so as to further translate the present findings into practical design recommendations for structural applications.

Acknowledgement

The authors gratefully acknowledge Jingru Zhang, Zhikang Feng, and others from the Nanjing Forestry University for assisting in various capacities.

Funding Statement

This work was supported by the National Natural Science Foundation of China (No. 51878354), the Natural Science Foundation of Jiangsu Province (No. BK20181402), Forestry Science and Technology Innovation and Promotion Project of Jiangsu Province (No. LYKJ [2024]08), 333 talent high-level projects of Jiangsu Province. All research outcomes presented in this paper are those of the writer(s) and do not necessarily reflect the views of the foundations.

CRediT authorship contribution statement

Yuxuan Wang: Investigation, Formal analysis, Writing - original draft. **Haitao Li:** Conceptualization, Funding acquisition, Supervision, Investigation, Formal analysis, Writing - original draft. **Yijia Guo:** Investigation, Formal analysis, Writing - original draft. **Jingru Zhang:** nvestigation, Formal analysis, Writing - original draft. **Haitao Ke:** Investigation. **Pin Zhou:** Investigation. **Yougui Luo:** Investigation. **Shang Zhao:** Investigation. **Rodolfo Lorenzo:** Formal analysis, Writing - original draft.

Conflicts of Interest

The authors declare that they have no known competing financial interests or personal relationships that could have appeared to influence the work reported in this paper.

Data Availability Statement

The datasets generated and analysed during the current study are available from the corresponding author on reasonable request.

References

[1] B. Shan, G. Wang, P. Lei, et al., Experimental research on formaldehyde emission characteristics from glubam by climate chamber test, Sustain. Struct 2023; 3: 27. https://doi.org/10.54113/j.sust.2023.000027.

[2] H. Li, B. J. Wang, L. Wang, et al., Characterizing engineering performance of bamboo-wood composite cross-laminated timber made from bamboo mat-curtain panel and hem-fir lumber, Compos. Struct 2021; 266: 113785. https://doi.org/10.1016/j.compstruct.2021.113785.

[3] R. Yadav, J. Kumar, Engineered wood products as a sustainable construction material: A review, In: IntechOpen, 2021. https://doi.org/10.5772/intechopen.97232.

[4] L. Han, A. Kutnar, J. Sandak, et al., Adhesive- and metal-free assembly techniques for prefabricated multi-layer engineered wood products: A review on wooden connectors, Forests 2023; 14 (2): 311. https://doi.org /10.3390/f14020311.

[5] A. Dauletbek, H. Li, R. Lorenzo, A review on mechanical behavior of laminated bamboo lumber connections, Compos. Struct 2023; 313: 116898. https://doi.org/10.1016/j.compstruct.2023.116898.

[6] X.T. Wang, E.C. Zhu, S. Niu, et al., Analysis and test of stiffness of bolted connections in timber structures, Constr. Build. Mater 2021; 303: 124495. https://doi.org/10.1016/j.conbuildmat.2021.124495.

[7] M. Chybiński, Ł. Polus, Experimental and numerical investigations of aluminium-timber composite beams with bolted connections, Structures 2021; 34: 1942–1960. https://doi.org/10.1016/j.istruc.2021.08.116.

[8] X. Zhang, H. Yin, E. Zhao, et al., Experimental investigation on embedment strength of bamboo-based composite prepared with the inorganic adhesive, J. Build. Eng 2023; 76: 107323. https://doi.org/10.1016/j.jobe.2023.107323.
[9] J. Wang, Y. Zhang, W. Yu, An in-depth study of the strengthening mechanism in wood scrimber prepared via roller-pressing impregnation technology, Constr. Build. Mater 2024; 457: 139413. https://doi.org/10.1016/j.conbuildmat.2023.134413.
[10] Q. Gao, Q. Lin, Y. Huang, et al., High-performance wood scrimber prepared by a roller-pressing impregnation method, Constr. Build. Mater 2023; 368: 130404. https://doi.org/10.1016/j.conbuildmat.2022.130404.
[11] G. Wu, Y. Zhang, Y. Zhong, et al., Size effect on the compressive strength of a novel structural wood composite: High-performance wood scrimber, Ind. Crops Prod 2024; 221: 119381. https://doi.org/10.1016/j.indcrop.2024.119381.
[12] M.J. He, J. Zhang, Z. Li, et al., Production and mechanical performance of scrimber composite manufactured from poplar wood for structural applications, J. Wood Sci 2016; 62: 429–440. https://doi.org/10.1007/s10086-016-1568-1.
[13] Y. Luo, H. Li, H. Ke, et al., Research on the basic mechanical properties of eucalyptus wood scrimber, Constr. Build. Mater 2025; 467: 140366. https://doi.org/10.1016/j.conbuildmat.2024.140366
[14] Q. Cao, Y. Wei, S. Chen, et al., Experimental investigations on the load-bearing properties of dowel connection joints of bamboo scrimber, Structures 2023; 50: 1868–1878. https://doi.org/10.1016/j.istructruc.2023.02.046.
[15] S. Ji, Q. Mou, G. Yuan, et al., Dowel–bearing behavior of bamboo scrimber for bolted–type joint, Ind. Crops Prod 2023; 193: 116178. https://doi.org/10.1016/j.indcrop.2022.116178.
[16] T. Ling, H. Li, G. Cheng, et al., Perpendicular-to-grain dowel-bearing strength behavior of side pressure laminated bamboo lumber, Structures 2023; 48: 754–767. https://doi.org/10.1016/j.istruc.2022.12.086.
[17] L.M. Ottenhaus, Z. Li, K. Crews, Half hole and full hole dowel embedment strength: A review of international developments and recommendations for Australian softwoods, Constr. Build. Mater 2022; 344: 128130. https://doi.org/10.1016/j.conbuildmat.2022.128130.
[18] K.E. Udele, J.J. Morrell, A. Newton, et al., Evaluation of dowel bearing strength of fungal-decayed cross-laminated timber, Wood Mater. Sci. Eng 2024; 19(3): 564–572. https://doi.org/10.1080/17480272. 2023.2266668.
[19] J.W. Gikonyo, M. Schweigler, T.K. Bader, Exploring the relationship between embedment behaviour in cross-laminated timber and its layers: An experimental study, Eng. Struct 2024; 318: 118677. https://doi.org/10.1016/j.engstruct.2024.118677.
[20] D. Yang, H. Li, C. Hong, et al., Performance of single-bolted laminated flattened-bamboo connection with steel plate under compression parallel to grain – An experimental and numerical study, Constr. Build. Mater 2023; 401: 132774. https://doi.org/10.1016/j.conbuildmat.2023.132774.
[21] C. Hong, H. Li, D. Yang, et al., Laminated bamboo lumber in compression perpendicular to the grain direction: Experimental investigation and the finite element analysis, Wood Mater. Sci. Eng 2023; 18(4): 1326-1339. https://doi.org/10.1080/17480272.2022.2104033.
[22] Y. Leng, M. Wang, Q. Xu, et al., Experimental study on longitudinal embedding performance of bolted engineered bamboo connections, Constr. Build. Mater 2024; 411: 134730. https://doi.org/10.1016/j.conbuildmat.2023.134730.
[23] V. Karagiannis, C. Málaga-Chuquitaype, A.Y. Elghazouli, Modified foundation modelling of dowel embedment in glulam connections, Constr. Build. Mater 2016; 102: 1168–1179. https://doi.org/10.1016/j.conbuildmat.2015.09.049.
[24] ASTM International, ASTM Committee D07 on Wood, Subcommittee AS. Standard test methods for small clear specimens of timber. ASTM international, 2014.
[25] X. Sun, M. He, Z. Li, Novel engineered wood and bamboo composites for structural applications: State-of-art of manufacturing technology and mechanical performance evaluation, Constr. Build. Mater 2020; 249: 118751. https://doi.org/10.1016/j.conbuildmat.2020.118751.
[26] T. Wang, Y. Wang, R. Crocetti, et al., In-plane mechanical properties of birch plywood, Constr. Build. Mater 2022; 340: 127852. https://doi.org/10.1016/j.conbuildmat.2022.127852.
[27] D. Yang, H. Li, Z. Xiong, et al., Mechanical properties of laminated bamboo under off-axis compression, Compos. Part A Appl. Sci. Manuf 2020; 138: 106042. https://doi.org/10.1016/j.compositesa.2020.106042.
[28] H. Li, H. Zhang, Z. Qiu, et al., Mechanical properties and stress strain relationship models for bamboo scrimber, J. Renew. Mater 2020; 8 (1): 13–27. https://doi.org/10.32604/jrm.2020.08779.
[29] R. Widmann, J.L. Fernandez-Cabo, R. Steiger, Mechanical properties of thermally modified beech timber for structural purposes, Eur. J. Wood Wood Prod 2012; 70(6): 775–784. https://doi.org/10.1007/s00107-012-0616-2.
[30] American Society for Testing and Materials. Standard Test Method for Evaluating Dowel-Bearing Strength

of Wood and Wood- Based Products, ASTM D5764, US; 2018. https://doi.org/10.1520/D5764-97R18

[31] I. Smith, A. Asiz, M. Snow, et al. Possible Canadian/ISO approach to deriving design values from test data[C]//CIB-W18 Meeting in Florence. 2006.

[32] M. Zhang, H. Fan, W. Li, et al., Experimental investigation on the dowel-bearing properties of neosinocalamus affinis-based bamboo scrimber, Eng. Struct 2024; 304: 117618. https://doi.org/10.1016/j.engstruct.2024.117618.